International Journal of Engineering Trends and Technology
ISSN: 2231–5381 / https://doi.org/10.14445/22315381/IJETT-V72I11P130

Volume 72 Issue 11, 307-321, November 2024

Original Article

Hybdeefu-Feaseg: A Comprehensive Framework For Lung Cancer Detection Combining Deep Learning, Fuzzy Logic, And Optimized Feature Selection

N. Raghapriya[1], Y. Kalpana[2]

[1,2] *Department of Computer Science, Vels Institute of Science Technology and Advanced Studies, Chennai, India.*

[1]*Corresponding Author : raghapriyakamal@gmail.com*

Received: 25 May 2024 Revised: 07 October 2024 Accepted: 17 October 2024 Published: 29 November 2024

Abstract *- Lung carcinoma is one of the greatest threatening and life-taking diseases in the globe, with the highest mortality rate. Early diagnosis and treatment can save lives. Among all of the diseases being investigated, lung cancer requires more focus because it impacts both men and women and raises the rate of death. Although MRI is the greatest scanning technology in the healthcare industry, it is difficult for doctors to comprehend and identify cancer from MRI (Magnetic Resonance Imaging) scans. In order to precisely detect malignant cells, computer-aided diagnostics might be beneficial for clinicians. Several studies and applications of computer-aided methods employ image processing and machine learning. Early and accurate diagnosis of malignant tumors can significantly enhance both the effectiveness of treatment and the persistence rate of carcinoma patients. Nevertheless, the conventional strategies' limited sensitivity, high cost, and disruptive characteristics constrain the applicability. Standard lung tumor forecasting techniques could not sustain precision because of low picture quality, interfering with the segmentation process. This research proposes a Hybrid Deep Learning and Fuzzy Logic Integration (HYBDEEFU-FEASEG) approach for Lung Cancer Detection. The projected model will include five major phases: The gathered raw MRI image was pre-processed via Gaussian filtering. The segNet method was proposed for segmentation. Haralick Texture Features (contrast, correlation, energy, and entropy), Local Phase Feature (LPF), and Shape feature (Hu moments, Zernike moments) techniques were used to extract texture features from segmented images. Artificial Gorilla Troops Optimization (AGTO) and Seagull Optimization Algorithm (SOA) approaches were developed for feature selection. The final detected outcomes (presence/absence of lung cancer) will be acquired from fuzzy logic. This method was used to classify and detect lung cancer more accurately. Therefore, our research targets to increase the efficiency of the existing model.*

Keywords *- Lung cancer, Hybrid deep learning and Fuzzy logic integration, SegNet, Artificial gorilla troops optimization, Seagull optimization algorithm.*

1. Introduction

Lung cancer will cause 1.8 million deaths worldwide in 2020, according to the World Health Organization (WHO). The lack of early detection tools and the late diagnosis of lung cancer is mostly to blame for the disease's high mortality rate [1]. This is mainly caused by increased smoking behaviours, a diagnosis of COPD, and Personal encounters with cancer. Because doctors undergo a lengthy theoretical procedure and cannot be instantly enhanced, the detecting method must initially be adjusted to increase the overall mortality rate in underdeveloped regions and nations [2]. The lung is a common target for radiation exposure due to its enormous surface area. These diseases are one with a greater occurrence of solid tumours, according to the data from the cohort of people who survived the atomic bomb, and it is expected to be the foremost source of death for both men and woman kind [3]. Globally, lung cancer is ranked seventh for women and second for men. These studies provide general information about the systematic approach to locating Lung Cancer, which has four fundamental phases. Following colorectal and breast cancers, this illness is the third maximum common malignancy among women [4]. Radiologists can create preoperative planning and prognosis evaluation using lung cancer Computer-Aided Diagnostic (CAD) systems' objective and precise diagnosis outcomes. Two elements make up a typical CAD system: (i) CADe subnetwork for identifying suspicious nodules and (ii) CADx subnetwork for assessing malignancy at the nodule and patient levels [5]. It can be treated only if lung cancer is found in its earliest stages. Some technologies, such as Computed Tomography, isotope, X-ray, and MRI, can be used to diagnose it [6]. Diagnostic imaging demonstrates that computed tomography is a thriving analysis method due to the sequential examination of the lung's soft tissues and

organs and the delivery of useful information about the damaged section. This is in comparison to additional imaging techniques like MRI and PET [7]. Both patients and medical personnel can benefit from early cancer discovery and the ability to forecast the depth of cancer survivorship to more effectively control expenditures, the severity of therapy, and the amount of time spent receiving medical care. Better chances for positive outcomes are realized when such sickness is detected early. Due to these factors, researchers studying the medical field, artificial intelligence, and medical experts are all very interested in the issue of cancer survivability [8]. The topic of lung nodule identification has significant clinical significance and scientific value. Lung nodules can be categorized into three sections according to characteristics: ground glass thickness nodules, compact nodules, and half-solid nodules [9]. Patients with bronchogenic carcinoma scheduled for VATS face difficult circumstances prior to surgery (such as medical damage, anaesthesia exposure, and the possibility of death), which may make them more nervous. Therefore, it is crucial to investigate what causes preoperative anxiety in lung carcinoma patients receiving VATS to find mitigation techniques [10]. The practice of using medication or dietary changes to leisurely or stop the development of precancerous into severe lung carcinoma is known as chemoprevention [11].

Deep learning techniques can be divided into four groups: autoencoders, Restricted Boltzmann Machines (RBMs), CNN-based techniques, and neuro-fuzzy techniques [12]. Fuzzy set theory quantifies the qualitative aspects and is connected to a collection of items with imperceptible borders and reasoning using natural language. We use ideas called membership degrees to characterize object memberships in any of these groupings [13]. Fuzzy logic and fuzzy set theory are the related and highly applicable basis for knowledge-based structures in prescription drugs for responsibilities like the detection and treatment of illness. Fuzzy logic is used in some areas, including the diagnosis of various kinds of carcinoma, including lung, skin, breast, prostate, and other malignancies [14]. Deep learning has become a viable method for automatically identifying and categorizing lung nodules in human data. DL algorithms have been used in numerous investigations based on human CT data. These have demonstrated that, when used on annotated archives of clinical scans, DL techniques can detect lung nodules with a higher degree of precision, sensitivity, and specificity [15]. The document follows a well-organized structure. Section 1 introduces the research topic, Section 2 provides an extensive literature review of prior methods, and Section 3 summarises the proposed methodology. Section 4 discusses the research results, and Section 5 concludes the study.

2. Literature Review

In 2022, Talukder et al. [16] recommended a hybrid ensemble feature extraction standard to categorize colon and lung carcinoma excellently. For datasets of cancer images, it combines deep feature extraction, ensemble learning, and high-yielding filtering. The study's findings indicate that a hybrid model has accuracy rates for lung, colon, and bronchial along with colon lung carcinoma detection of 99.05%, 100%, and 99.30%, respectively. Therefore, these models might be used in clinics to assist doctors in making cancer diagnoses. In 2022, Qazi et al. [17] concluded that the danger of developing lung carcinoma will be ascertained, and patients will be given instructions to eliminate the danger. After obtaining the hazard value for bronchogenic carcinoma, the state of the patient's vulnerability and struggle with anxiety is utilized to determine the impacts of stress on the disease. The neuro-fuzzy logic model has been offered as a solution to the issue. This study allows these folks to take precautions to lower their cancer risk. This study will also look at using neuro-fuzzy logic models in artificial intelligence and health-related fields. In 2023, Ding et al. [18] proposed a Convolutional Neural Network and transformer-based fuzzy fusion technique that uses the features extracted through a Convolutional Neural Network and Transformer together via an entirely novel fuzzy fusion segment. The improved segmentation results from the new model's use of deconvolution to produce the final segmentation result. The investigational outcomes on the Chest X-ray and Kvasir-SEG datasets demonstrate that FTransConvolutional Neural networks outperform the most advanced deep segmentation models in segmentation tasks.

In 2023, Valerian et al. [19] explored a Machine Learning mechanism of the type automatic encoder for irregularity identification created via PyTorch was trained using 34 optimal IMRT treatment plans and 10 suboptimal Intensity Modulated Radiation Therapy treatment plans collected from Siloam MRCCC Semanggi Hospital. This study was divided into four stages: planning, development, validation, and evaluation. The findings suggest that the majority of radiomic features are noise that must be eliminated for the model to identify treatment options that are not optimal. In 2020, Li et al. [20] introduced wavelet dynamic examination, which was utilized to extract and restore the lung parenchyma, apart from noise intrusion from external the lung parenchyma. Accurately find the lung nodules with the aid of the algorithm. The characteristics of the *computerized tomography* picture of the pulmonary nodules are then extracted using the CNN enhanced by genetic procedure and the conventional CNN. It can be shown from a comparison of the two algorithms' accuracy levels that the convolutional neural network improved using genetic process performs better. A convolutional neural network augmented by a genetic procedure is utilized to distinguish and categorise the existing pulmonary nodule images, which gives instructions for pulmonary nodule CT picture discovery expertise. In 2023, Ardimento et al. [21] suggested an innovative method for computer tomography scans-based accurate 3D lung nodule detection. This study

uses an evolutionary method to create different iterations of the UNet-based structure, known as GUNet3++, to identify patients with bronchogenic carcinoma from examining lung computerized tomography scan pictures. The method is verified on the LIDC-Image Database Resource Initiative actual dataset, and the findings reveal that it produces better 3D models of lesions by increasing the segmentation quality metrics like IoU and Dice over baselines. In 2022, Hua et al. [22] examined small extracellular vesicles as a biological indicator for the initial recognition of bronchogenic carcinoma using a new type of autoantibody. The Small Extracellular Vesicles were purified from plasma by ultracentrifugation, and their morphology and characteristic markers were used for validation. Additionally, binding assays, Nanoflow cytometry, and immunogold labelling transmission electron microscopy demonstrated that the rheumatoid factors may attach to the antiserums on SEVs, which may account for the autoantibodies seen on SEVs. Additionally, the connection reduced complement-mediated cytotoxicity, which may help lung cancer elude the immune system.

In 2022, Ahmad et al. [23] proposed a novel technique known as Cancer Cell Detection using Hybrid Neural Network for an initial and precise analysis. Acutting-edge 3D-convolution neural network was also used in this study to increase diagnosis precision. The proposed method also makes it possible to differentiate between benign and malignant haemorrhaging. The suggested hybridDL strategy for early lung cancer evaluation is viable when the findings are analyzed using conventional statistical methods. In 2019, Nasrullah et al. [24] suggested the accurate diagnosis of malignant nodules, a brand-new deep learning-based model with numerous techniques. Faster R-Convolutional Neural Networks were utilized to distinguish nodules via expeditiously learned qualities from CMixNet and U-Net, such as encoder-decoder structure. The 3D CMixNet structure's learned characteristics were used to classify the nodules utilizing a GBM. In initial-phase bronchogenic carcinoma diagnosis, the DL model for nodule recognition and organization, in conjunction with scientific variables, helps to lessen misdiagnosis and false positive outcomes. On LIDC-IDRI datasets, the suggested system was assessed for sensitivity (94%) and specificity (91%), and improved outcomes were obtained when associated with the current approaches. In 2021, Naik et al. [25] investigated 108 research publications to examine deep learning approaches' role in identifying malignant tumours in lung CT scans. Variations applied to deep learning architecture are discussed in this study to increase the classification system's accuracy and thoroughly compare all DL methods presently used for classifying lung nodules. Sorting lung nodules via sophisticated DL techniques also poses obstacles and potential in this study. The report concludes that the goal is to identify the malignant lesion early and address new challenges in nodule categorization. In 2020, Bicakci et al. [25] suggested the molecular imaging-based sub-classification of lung cancer. Adenocarcinoma (ADC) and Squamous Cell Carcinoma (SqCC), two subtypes of NSCLC, were distinguished in that study using deep learning-based classification algorithms, which were thoroughly studied.

3. Proposed Methodology

This study demonstrates the efficacy of deep learning and image processing technology in accurately classifying and forecasting bronchogenic carcinoma. The anticipated model will have five key stages:

(a) pre-processing, (b) segmentation, (c) feature extraction, (d)feature selection and (e) lung cancer detection.
The total flow diagram of the suggested model is in Figure 1

3.1. Pre-processing

This research will pre-process the gathered raw MRI images through gaussian filtering and contrast stretching for image contrast enhancement. To overcome the noise in the image, efforts need to be made to improve the quality of the image, one of which is by filtering the image. There are many image filtering techniques, and the authors used spatial domain filtering techniques in this study. A spatial domain is a filtering technique based on manipulating a pixel set of an image to generate a new image. There are different types of filters in the spatial domain, namely nonlinear and linear filters. In this study, the authors used a linear mean filter. The mean filter smooths and eliminates noise by replacing the values at the midpoint of the entire matrix in the image with the average value on the damaged image. Gaussian filter uses a non-local mean filter that can preserve subtle grey-values and edge information. Their filter selects pixels similar to the corrected pixel and applies a weighted average function within a small fixed window. Therefore, the Gaussian filter on the rendered images increases the similitude of synthetic images to real images. These methods are described below:

3.1.1 Gaussian Filtering

It is a linear filter. This filter is often applied to blur the image or minimize noise. Gaussian filtering is more effective at smoothing images. In one dimension, the Gaussian function is defined as follows:

$$G(x) = \frac{1}{\sqrt{2\pi\sigma^2}} e^{\frac{-x^2}{2\sigma^2}} \quad (1)$$

Where, σ is the standard deviation. The behaviour of the Gaussian function is significantly influenced by its standard deviation. The Gaussian function, which computes the values inside the kernel, is expressed in the following Equ (2)

$$G(x) = \frac{1}{\sqrt{2\pi\sigma^2}} e^{\frac{-x^2+y^2}{2\sigma^2}} \quad (2)$$

Where x represents the worth of x-coordinate, y is the value of y-coordinate, and σ denotes standard deviation.

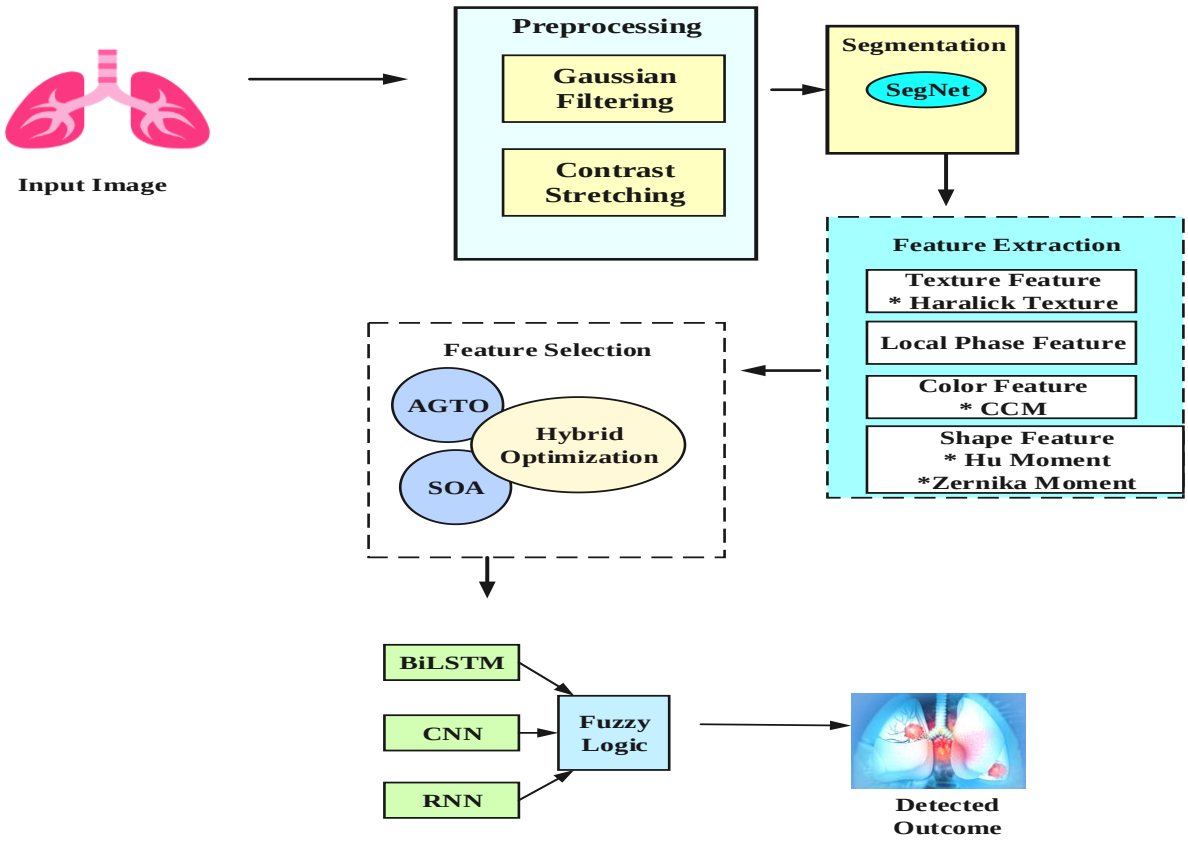

Fig. 1 Overall workflow diagram of the proposed model

3.1.2. Contrast Stretching

Low dynamic range in the image sensor, poor illumination, or even the incorrect lens aperture setting during the image capture phase can all lead to low contrast images. Contrast stretching is a procedure that increases the range of intensity levels in a picture, covering the whole intensity range of the display mechanism or recording medium. In order to boost the contrast of an image, the dark areas are made darker, and the bright areas are made brighter. Equation (3) represents a transformation used to achieve contrast stretching.

$$S = \begin{cases} l * r & 0 \le r < a \\ m * (r-a) + v & a \le r < b \\ n * (r-b) + w & a \le r < b \end{cases} \quad (3)$$

Where, $m, l, and\ r$ are represents slopes. By applying a slope of less than one, the dark grey levels get darker. The contrast stretching transformation increases the dynamic range of the altered image. In accordance with an input image and purpose of usage, several slopes can be applied. Image enhancement is a subjective processing approach since no set of slope values will provide the desired outcome.

$$\begin{cases} 0 & if\ r \le a \\ L-1 & if\ r > a \end{cases} \quad (4)$$

The output of the thresholding function is always a binary image with two colours, black (pixel value 0) and white (255).

3.2. Segmentation

Our research used a SegNet methodology to segment pre-processed lung cancer images precisely. This approach enabled us to identify Regions of Interest (ROIs) within the images. By harnessing advanced segmentation techniques, our research aimed to enhance the accuracy and efficiency of detecting these critical ROIs, ultimately contributing to improved diagnosis and treatment planning for lung cancer patients.

3.2.1. SegNet

The segmentation of medical semantic images was successfully handled by SegNet architecture, also known as CNN encoder-decoder. It has five symmetric decoders and five encoders, batch normalization, convolution layers, rectified linear unit layer, upsampling, SoftMax classifier, and max-pooling layer, as shown in Figure 2. After each convolutional layer, the encoder and decoder systems employ batch normalisation. It is convolutional since there is no entirely connected layer. Respectively, each and every encoder layer has a matching decoder layer to enhance the SegNet strategy.

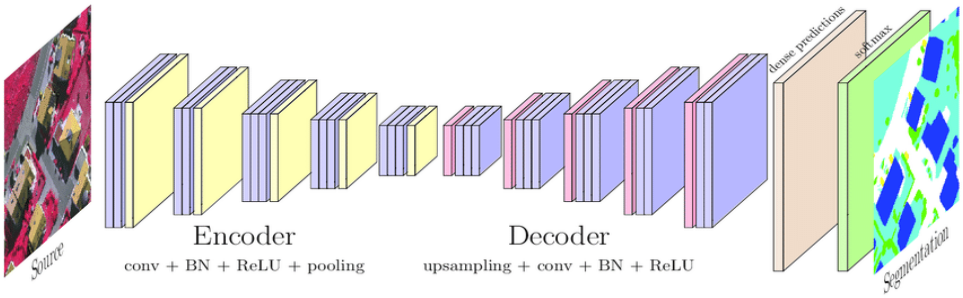

Fig. 2 Architecture of SegNet

Therefore, the decoder network for VGG-19 and VGG-16 comprises 16 and 13 convolutional layers, respectively. The encoder is used as VGG-16 or VGG-19, which gradually reduces an image's spatial dimension by pooling layers per the CNN encoder-decoder concept. The VGG-19 system is more wide-ranging than the VGG-16 system. All convolutional layers are supplemented by tiny 3x3 filters that reduce the parameters in each layer. This VGG-19 system has developed robust attribute illustrations for various images. In order to create a sparse feature map, a decoder is employed to upsample its input via the pool guides transmitted from its encoder. Convolution is then carried out to measure the density of the feature maps utilizing a trainable filter bank.

A Softmax classifier is assumed to be the last decoder outcome characteristic maps for pixel-by-pixel organization. The decoder improved spatial dimensions to enable rapid and precise picture segmentation. Most recent deep architectures for segmentation have identical encoder networks, i.e. VGG16, but differ in the form of the decoder network, training and inference. The role of the decoder network is to map the low-resolution encoder feature maps to full input-resolution feature maps for pixel-wise classification.

Although all these factors improve performance on challenging benchmarks, it is unfortunately difficult from their quantitative results to disentangle the key design factors necessary to achieve good performance. The novelty of SegNet lies in how the decoder upsamples its lower-resolution input feature map(s). Specifically, the decoder uses pooling indices computed in the max-pooling step of the corresponding encoder to perform non-linear upsampling. This eliminates the need for learning to upsample. The upsampled maps are sparse and convolved with trainable filters to produce dense feature maps.

3.3. Feature Extraction

The process of collecting features, such as texture, colour, and shape, from an image is known as feature extraction. This research extracts the segmented image using techniques such as Local Phase Feature (LPF), Haralick Texture Features, Hu moments, Zernike moments, and shape feature extraction.

3.3.1. Haralick Texture Features

Human visual perception depends extensively on texture. Statistical texture methods compute resident qualities at each place in the picture and obtain conventional statistics from the supplies of the local characteristics to analyse the spatial distribution of grey standards. 1973, Haralick et al. presented textural characteristics and the Grey Level Cooccurrence Matrix. This technique has been widely employed in image analysis applications, mainly in the biomedical sector. There are two procedures for extracting features. The first phase involves computing the GLCM; the second involves computing the texture features based on the GLCM. According to the grey level, the GLCM displays the frequency of each grey level at a pixel in relation to each other at a set geometric point. The measurement of these factors is discussed below:

i. Contrast

Contrast measures the intensity or grey level variances between the reference pixel and its neighbor. The huge contrast in GLCM represents huge intensity variations. It is shown in Equation (5)

$$contrast = \sum_i \sum_j (i-j)^2 P_d(i,j) \quad (5)$$

ii. Correlation

The correlation feature shows that grey level values in the cooccurrence matrix are linearly dependent. This function is expressed in Equation (6)

$$correlation = \sum_i \sum_j P_d(i,j) \frac{(i-\mu_x)(j-\mu_y)}{\sigma_x \, \sigma_y} \quad (6)$$

Where, μ_x, μ_y are mean values, and σ_x, σ_y are standard deviations. μ_x *and* μ_y are expressed in the following equation.

$$\mu_x = \sum_i \sum_j i P_d(i,j) \;\; ; \;\; \mu_y = \sum_i \sum_j j P_d(i,j) \quad (7)$$

The standard deviations σ_x, σ_y are given in Equation (8)

$$\sigma_x = \sqrt{\sum_i \sum_j (i-\mu_x)^2 P_d(i,j)} \;\; ; \;\; \sigma_y = \sqrt{\sum_i \sum_j (i-\mu_y)^2 P_d(i,j)} \quad (8)$$

iii. Energy

The Angular Second Moment (ASM) provides energy. ASM measures the local homogeneity of grey levels. The

ASM value will be high if the pixels are quite similar. The expression of energy is described in Equation (9)

$$Energy = \sqrt{ASM} \quad (9)$$

Where, $ASM = \sum_i \sum_j (P_d)^2(i,j)$ (10)

iv. Entropy

An image's degree of disorder or unpredictability is measured by its entropy. When the cooccurrence matrix's elements are evenly distributed, the entropy value is greatest; when they are not, it is lowest. It is expressed in the following Equation (11)

$$Entropy = -\sum_i \sum_j P_d(i,j)\, ln\, P_d(i,j) \quad (11)$$

3.3.2. Local Phase Feature

A 3-D phase symmetry measure from odd and even symmetric log-Gabor filter replies can be represented by o_{rm} , e_{rm}, correspondingly, remunerated by a noise power threshold T_r. The phase symmetry feature is expressed in the following Equation (12)

$$PS = \frac{\sum_r \sum_m \lfloor [|e_{rm}| - |o_{rm}|] \rfloor - T_r}{\sum_r \sum_m \sqrt{e_{rm}^2 + o_{rm}^2 + \varepsilon}} \quad (12)$$

Let G (x, y): $N_x \times N_y \to Z$ be the grey levels of an $N_x \times N_y$ images I for Z = 0 to 255. In order to create the four distinct patterns represented by the number m of motif, pixel G (x, y) is split into four blocks, each containing two two-pixel grids. These four motifs will be stored as four $N_x \times N_y$ two-dimensional motifs of scan pattern matrix P_i [x, y], where i = 1, 2, 3, 4, x = 1, 2...,N_x , y = 1, 2..., N_y, and Pi [x, y]: $N_x \times N_y \to w$ signifies a $N_x \times N_y$matrix for W = 0 to 6. The CCM computes distribution within the two-dimensional matrix $P_i[N_x, N_y]$. The synchronisation that separates (x, y) on the x-axis in dx and y-axis in dy, then the total number of co-occurring motifs of scan pattern pairings (u, v) (where u = 0, 1,..., 6) is calculated. It is expressed in Equation (13).

$$M_i(u,v) = M_i(u,v \mid \delta_x, \delta_y) = M_i(P_i[x,y], P_i[x+\delta_x, y+\delta_y]) \quad (13)$$

Where, $P_i[x,y] = u$, $P_i[x+\delta_x, y+\delta_y] = v$. As illustrated in Equation (14), the co-occurring probabilities of number i motifs of the scan model matrix are calculated by dividing $M_i(u,v)$by the sum of all counts for u and v.

$$m[u,\ v] = \frac{M_i(u,v)}{N_i} \quad (14)$$

Where,

$$N_i = \sum_{u=0}^{6} \sum_{v=0}^{6} M_i(u,v); \qquad 1 \le i \le 4 \quad (15)$$

Thus, there will be a total of 7x7 two-dimensional CCM grids, or 7x7 = 49, where $Nf = 49$ is the total number of Colour Co-occurrence Matrix characteristics.

3.3.3. Shape feature extraction

In this study, shape features are extracted using Hu moments and Zernike moments. These two techniques are described below in detail:

i. Hu moments

This technique uses a statistical feature to extract visual information. Digital image recognition frequently makes use of moments in two dimensions. In actuality, it brings one-dimensional signal order moments into two-dimensional space. Moment theory was utilised to build and popularise a statistical feature extraction approach in image recognition. If the scaling factor $\rho \le 2$ and the trajectory graph's rotation angle are both $\theta = 45^0$degrees, the Hu moment may be assured. For the two-dimensional function $f(x,y) \in R^2$, which is defined on the plane $0 - xy.$, The following Equation (16) describes the $p+q$ order mixed origin moment:

$$p, q = 0, 1, 2 \cdots \quad (16)$$

The following formula defines the $p+q$ order of mixed central moment:

$$\mu_{pq} = \int_{-\infty}^{\infty} \int_{-\infty}^{\infty} (x-\bar{x})^p (y-\bar{y})^q f(x,y) d_x d_y \quad (17)$$

Where $\bar{x}, \bar{y}$ represents the gray centre of gravity for the image and it is expressed as:

$$\bar{x} = \frac{m_{10}}{m_{00}} \ ; \qquad \bar{y} = \frac{m_{01}}{m_{00}} \quad (18)$$

The normalized central moment function is defined in the following equation:

$$\eta_{pq} = \frac{\mu_{pq}}{\mu_{00}^r} \quad (19)$$

Under the constraints, $r = p + q + 2/2$; $p + q = 0,1,2,3 \cdots$

The seven moment functions are built utilising the aforementioned core moments. These 7 expressions represent translation, scaling, and rotation. These are expressed in the following Equation (20)-(26)

$$\emptyset_1 = \eta_{20} + \eta_{02} \quad (20)$$

$$\emptyset_2 = (\eta_{20} - \eta_{02})^2 + 4\eta_{11}^2 \quad (21)$$

$$\emptyset_3 = (\eta_{30} - 3\eta_{12})^2 + (\eta_{03} - 3\eta_{21})^2 \quad (22)$$

$$\emptyset_4 = (\eta_{30} + \eta_{12})^2 + (\eta_{03} + \eta_{21})^2 \quad (23)$$

$$\emptyset_5 = (\eta_{30} - 3\eta_{12})\ \eta_{30} + \eta_{12})\big[(\eta_{30} + \eta_{12})^2 - 3(\eta_{03} + \eta_{21})^2 + (3\eta_{21} - \eta_{03})(\eta_{03} + \eta_{21})[3(\eta_{30} + \eta_{12})^2 - (\eta_{03} + \eta_{21})^2]\big] \quad (24)$$

$$\emptyset_6 = (\eta_{20} - \eta_{02})[(\eta_{30} + \eta_{12})^2 - (\eta_{03} + \eta_{21})^2] + 4\eta_{11}(\eta_{30} + \eta_{12}) + (\eta_{03} + \eta_{21}) \quad (25)$$

$$\emptyset_7 = (3\eta_{21} - \eta_{03})(\eta_{30} + \eta_{12})[(\eta_{30} + \eta_{12})^2 - 3(\eta_{03} + \eta_{21})^2] + (3\eta_{12} - \eta_{30})(\eta_{03} + \eta_{12})[3(\eta_{03} + \eta_{21})^2 - (\eta_{03} + \eta_{21})^2] \quad (26)$$

ii. Zernike Moment

A unique type of complex moment known as a Zernike moment is built on orthogonal functions known as Zernike polynomials. Zernike moments have better benefits in terms of their expressive power and noise sensitivity than HU moments, but they have a more difficult calculation. When it comes to target recognition, Zernike moments are frequently employed because of their rotation invariance properties. A group of orthogonal polynomials $V_{nm}(p,\theta)$, which are orthogonal in the unit circle $\rho \leq 1$, are presented by Zernike. The following steps are used to produce the polynomial function in polar coordinates:

$$V_{nm}(\rho,\theta) = R_{nm}(\rho) \exp(im\theta) \quad (27)$$

Under the constraints, $n = 0, 1, 2 \cdots and\ m = 0, \pm1, \pm2 \cdots, |M| \leq n\ , where\ (n - |M|)$ represents an even number. ρ denotes the vector form of origin point to pixel point (x, y), θ specifies the angle between the vector ρ and $x\ axis$, $R_{nm}(\rho)$ is radial polynomial.

$$R_{nm}(\rho) = \sum_{s=0}^{(n-|m|)/2} (-1)^5, \frac{(n-s)!\, p^{(n-2s)}}{S!((n-2s+|m|)/2)!\ ((n-2s-|m|)/2)!} \quad (28)$$

Radial polynomials $R_{nm}(\rho)$ satisfy the following Eq.(29)

$$\int_0^l R_{nl}(r) R_{ml}(r)\ \rho d\rho = \frac{1}{2(n+1)} \delta_{nm} \quad (29)$$

Where, δ_{nm} denotes Kronec ker delta.

The orthogonality conditions of Zernike polynomials are expressed in the following equation:

$$\int_0^{2\pi} \int_0^l V_{nl}^*(r) V_{mk}(p,\theta) \rho d\rho d\theta = \frac{1}{2(n+1)} \delta_{nm} \delta_{lk} \quad (30)$$

In the above Equation (30), * denotes complex conjugate, and this equation is simplified to the following Equation (31).

$$V_{nm}^*(\rho,\theta) = V_{n-m}(\rho - \theta) \quad (31)$$

Important properties of R_{nm} as follows:

$$R_{nm}(1) = 1, \qquad R_{nm}(r) = \rho^n;\ R_{00}(\rho) = 1 \quad (32)$$

The following Equation (33) defines a n order Zernike polynomial with a repeating rate of M:

$$A_{nm} = \frac{n+1}{\Pi} \iint \rho^2 \leq 1\, f(\rho,\theta) V_{nm}^*(\rho,\theta) \rho\rho d\theta,\ \rho^2 \leq 1 \quad (33)$$

For digital images, the integral is replaced by summation, and it is given by:

$$A_{nm} = \frac{n+1}{\pi} \sum_x \sum_y f(x,y)\, V_{nm}^*(\rho,\theta) dxdy, \qquad x^2 + y^2 \leq 1 \quad (34)$$

It is important to shift the axis trajectory image's centre to the coordinate circle and map the trajectory's pixel points onto the unit circle to compute the Zernike moments of an axis shaft orbit. It is clear from the formula that $V_{nm}^*(\rho,\theta)$ it can extract picture features and, for bigger n values, $V_{nm}^*(\rho,\theta)$can retrieve high-frequency characteristics. In cases when n is less, $V_{nm}^*(\rho,\theta)$ it yields low-frequency features. High moments may be built using Zernike moments. Theoretically, greater moments can store more picture data, improving pattern detection.

3.4. Feature Selection

The best features will be chosen from the retrieved features using a novel hybrid optimisation approach, which has been suggested. The conceptual improvement of the conventional Artificial Gorilla Troops Optimisation (AGTO) and Seagull Optimisation Algorithm (SOA) will be the proposed hybrid optimisation model in this research. In this phase, Artificial Gorilla Troops Optimization (AGTO) and Seagull Optimization Algorithm (SOA) approaches were created for FS. The best features will be chosen from the segmented lung image using a novel hybrid optimization approach, which has been suggested. FS can be viewed as an optimization issue with multiple objectives and two competing goals to be met: greater precision in classification and a reduced number of randomly chosen features. A solution is better if its feature count and classification accuracy are lower.

While the AGTO algorithm is a unique metaheuristic strategy based on gorilla group behavior, the SOA approach offers strong global searching capability. This study suggests two hybrid optimization methods to enhance the SOA algorithm's local search capability. Three different solutions are available in the AGTO method's optimizing stage: P is the gorilla's position, and G is the precise spot of the candidate gorilla produced at each step. It will operate if it performs better than the current one. Ultimately, the "silverback" is the superior choice in every iteration. First, one of the two algorithms is chosen randomly for optimization, much like a roulette wheel. The algorithm selects Equation 40 at random for this iteration's position update and uses the advantages of the two formulas to update the position, thus improving the optimization ability. To circumvent the local optimisation problem, this technique will randomly conduct global and local searches. This strategy is called SOA-AGTO.

3.4.1. Artificial Gorilla Troops Optimization (AGTO)

An artificial metaheuristic optimization system that mimics gorilla social behaviour is called the Artificial Gorilla Troop Optimization (AGTO) algorithm. AGTO has demonstrated its effectiveness when compared to other cutting-edge metaheuristic algorithms like TSA, GWO, SCA, MVO, WOA, GSA, and MFO by resembling the live practice of the Gorilla Troop. The primary distinction

between meta-heuristic algorithms is how they update existing algorithms with new answers. There are two steps to this process in the AGTO: Local based forward and Global based forward. In the subsection below, both phases are described:

i. Local based Forward

This is the first stage in the AGTO process. It is expressed in the following equation:

$$G_{new} = \begin{cases} (ub - lb) \times \theta_1 + lb, rdn < \tau \\ (\theta_2 - M) \times G_{rds} + N \times K, \quad rdn \geq 0.5 \\ G - N \times [N \times (G - G_{rds}) + \theta_3 \times (G - G_{rds})], rdn < 0.5 \end{cases} \quad (35)$$

Where, G represents the present location, G_{new} denotes the new location of the gorilla, $\theta_1, \theta_2, and\ \theta_3$ and generated random values in the interval 0 to 1. lb and ub are lower and upper limitations of search space. τ is the given operator, and it changes between 0 and 1. G_{rds} It specifies random gorilla picked up from the entire population. K, N, and M are expressed in Equations (36)-(38).

$$K = RD \times X \quad (36)$$

$$N = M \times l \quad (37)$$

$$M = Q \times \left(1 - \frac{h}{H}\right) \quad (38)$$

$$\text{Where, } Q = \cos(2 \times \theta_4) + 1 \quad (39)$$

From above Equation (36)-(38), N represents the control operator, and RD denotes the created random value of -M to M, l is the generated random value between -1 and 1, the letter h denotes the present iteration, Q is an amplifying factor, H represents the maximum quantity of iteration, and θ_4 denotes a random value between 0 and 1.

ii. Global Based Forward

The general form for global based forward is shown in below Equation (40)

$$G_{new} = \begin{cases} K \times I \times (G - SB) + G, M \geq \varepsilon \\ SB - (SB \times IF - G \times IF) \times VT, \ M < \varepsilon \end{cases} \quad (40)$$

Where, ε denotes the reference parameter, which is set before evaluation, SB represents the silverback gorilla location. VT specifies the violation term, which is given in Equation (41). IF is the impact term expressed in Equation (43), and I is the synthesis term specified in Equation (44).

$$VT = \rho \times RF \quad (41)$$

$$\text{Where, } RF = \begin{cases} U_1, \ rdn \geq 0.5 \\ U_2, \ rdn < 0.5 \end{cases} \quad (42)$$

$$IF = 2 \times \theta_5 - 1 \quad (43)$$

$$I = \left(\left|\frac{1}{Pop}\sum_{i=1}^{Pop} G_i\right|^{\alpha}\right)^{\frac{1}{\alpha}} \quad ; \ \alpha = 2^k \quad (44)$$

3.4.2. Seagull Optimization Algorithm (SOA)

Seagulls are seabirds that are found all over the world and are formally referred to as the seagull family. There are numerous varieties of seagulls, each with a unique mass and length. Flies, trawl, serpents, amphibians, and fish worms are among the omnivorous foods that seagulls consume. Seagulls in a group can transfer toward the seagull with the highest unintended endurance or one whose fitness level is lesser than the others. The other seagulls can adjust their starting positions based on the fittest seagull. Following their avoidance of neighbor collisions, the search agents proceed toward the best neighbor, as equation (14) indicates.

$$M_S = B \times (P_{bs}(x) - P_s(x)) \quad (45)$$

In this case, MS stands for the search agent Ps location, with respect to the search agent Pbs, which fits the best. B's randomised behaviour ensures that exploration and exploitation are properly balanced. Since FS is a discrete optimization problem, the original AGTO is transformed here using a sigmoid transfer function, and the probability value is then calculated using Equation 46.

$$T\left(\Delta p_i^L(It+1)\right) = sigmoid\left(\Delta p_i^L(It+1)\right) = \frac{1}{1+e^{-2\Delta p_i^L(It+1)}} \quad (46)$$

The first update of each gorilla position is indicated by the notation (Δp_i^L (It+1)). In this case, a sigmoid function of transfer is used to transform the original AGTO and calculate the probability value because FS is a periodic problem for optimization. Ultimately, the AGTO algorithm's equation is refined to the SOA algorithm's seagull attack formula, enhancing the seagull algorithm's local discovery capability. The SOA-AGTO technique was developed to help gulls more easily approach their prey. Equation 47 provides its numerical formula.

$$M_s = B \times (P_{bs}(x) - P_s(x)) \times exp(-2\Delta p_i^L(It+1)) \quad (47)$$

To swiftly approach the target item $(-2\Delta p_i^L(It+1))$ swap the slight between objects. Therefore, the original AGTO is upgraded $(-2\Delta p_i^L(It+1))$ so seagulls can effectively approach prey.

4. Results and Discussion

The operation of the recommended technique was assessed using the IQ-OTH/NCCD lung carcinoma dataset. This data is set to two different values of 60 and 70 percentage for computation. The experiment was implemented in Python. Several metrices are used to analyze the efficiency of the proposed method, and they are discussed in the following section.

4.1. Evaluation metrics

Several accepted criteria were applied to estimate the performance of the suggested network, including Accuracy, Precision, Sensitivity, Specificity, TPR, FPR, TNR, F1 score,

and Recall. The efficiency of these metrics is discussed below:

4.1.1. Accuracy

The measure of correctness repeatedly labels the execution of the system across all classes. When every class is similarly significant, it is advantageous. It is resolute by dividing the total number of guesses by the number of accurate forecasts. It is expressed as follows:

$$Accuracy = \frac{TP+TN}{TP+TN+FP+FN} \quad (48)$$

Where, TP is True Positive, TN indicates True Negative, FP means False Positive, and FN denotes False Negative values.

4.1.2. Precision

The degree of precision is the ratio of Positive examples appropriately classified to all samples properly or erroneously recognised as Positive. The exactness gauges how exactly the standard categorizes a sample as positive. The mathematical expression of precision is given below:

$$Precision = \frac{TP}{TP+FP} \quad (49)$$

4.1.3. Sensitivity

It is a statistic that assesses how well a test can classify a positive outcome. It is determined by the percentage of true positives the test successfully discovered. The sensitivity equation is:

$$Sensitivity = \frac{TP}{TP+FN} \quad (50)$$

4.1.4. Specificity

Specificity is a crucial extra element for binary classification problems. It evaluates a model's ability to precisely identify negative events among all of the genuinely negative examples in the dataset.

$$Specificity = \frac{TN}{TN+FP} \quad (51)$$

4.1.5. True Positive Rate (TPR)

It is a functioning indicator employed in binary classification tasks to assess how effectively a model accurately distinguishes positive examples from all the real positive cases in the dataset. The mathematical expression of TPR is given below:

$$TPR = \frac{TP}{FP+FN} \quad (52)$$

4.1.6. False Positive Rate (FPR)

It is a performance indicator used in binary classification tasks to assess how frequently the model misidentifies negative examples as positive.

$$FPR = \frac{FP}{TN+FP} \quad (53)$$

4.1.7. True Negative Rate (TNR)

It is a performance indicator utilized in binary categorization tasks to assess how effectively a standard accurately distinguishes negative examples from all the true negative occurrences in the dataset.

$$TNR = \frac{TN}{FP+TN} \quad (54)$$

4.1.8. F1 Score

The F1 score, sometimes called the F-measure or F-score, is a well-liked statistic used in binary classification issues to balance the trade-off between recall (sensitivity) and precision. Accounting for both FS and FN offers a single number that sums up a model's performance.

$$F-measure = \frac{2\times(precision\times recall)}{precision+recall} \quad (55)$$

4.1.9. Recall

The recall is concluded as the proportion of positive samples that were properly recognized as positive for all positive examples. The recall gauges how healthy the system can detect Positive samples. The more positive samples that are acknowledged, the larger the recall. The calculation method of recall is shown below:

$$Recall = \frac{True\ Positive}{Actual\ Positive} \quad (56)$$

4.2. Performance Metrics Comparison

The proposed model Hybrid Deep Learning and Fuzzy Logic Integration for Lung Cancer Detection (HybDeeFu) was compared with various existing algorithms such as Artificial Gorilla Troops Optimization (AGTO) and Seagull Optimization Algorithm (SOA), Pro_classifier, CNN [27], RNN [28]. The model was implemented in python. The dataset is set with two different percentages for computation https://www.kaggle.com/datasets/hamdallak/the-iqothnccd-lung-cancer-dataset.

Table 1 evaluates several existing techniques with the proposed 60% trained dataset method. Table 2 illustrates the comparative analysis of the suggested approach with various techniques currently in practice, with datasets trained to 70%.

Figures 3 and 4 represent the findings for malignant and benign cases. Illustrative images are provided to present the application of contrast stretching, Gaussian Filter, normal image, malignant image, benign image and segmented lung cancer images. These visual representations offer valuable insights into the impact of these techniques on enhancing image quality and emphasizing significant features in various cases.

Table 1. Existing and proposed technique comparison for dataset trained with 60%

	AGTO	SOA	Pro_classifier	CNN [27]	RNN [28]	PROPOSED
Accuracy	0.955	0.935	0.919	0.876	0.911	0.977
Precision	0.935	0.903	0.879	0.816	0.867	0.969
Sensitivity	0.943	0.907	0.878	0.815	0.866	0.966
Specificity	0.943	0.961	0.919	0.917	0.923	0.963
TPR	7.000	4.656	3.625	2.204	3.250	10.50
FPR	0.033	0.048	0.060	0.092	0.066	0.016
TNR	0.965	0.951	0.939	0.907	0.933	0.983
F1 Score	0.934	0.905	0.877	0.810	0.869	0.956
Recall	0.943	0.907	0.878	0.815	0.866	0.966

Table 2. Comparison of the proposed model with existing techniques for dataset trained with 70%

	AGTO	SOA	Pro_classifier	CNN [27]	RNN [28]	PROPOSED
Accuracy	0.969	0.947	0.933	0.868	0.917	0.985
Precision	0.957	0.931	0.811	0.807	0.890	0.981
Sensitivity	0.954	0.921	0.911	0.803	0.875	0.978
Specificity	0.977	0.960	0.950	0.901	0.937	0.989
TPR	10.00	5.846	4.512	2.038	3.524	12.071
FPR	0.022	0.039	0.051	0.098	0.062	0.010
TNR	0.977	0.960	0.954	0.901	0.937	0.989
F1 Score	0.952	0.923	0.833	0.807	0.867	0.980
Recall	0.954	0.921	0.942	0.803	0.875	0.978

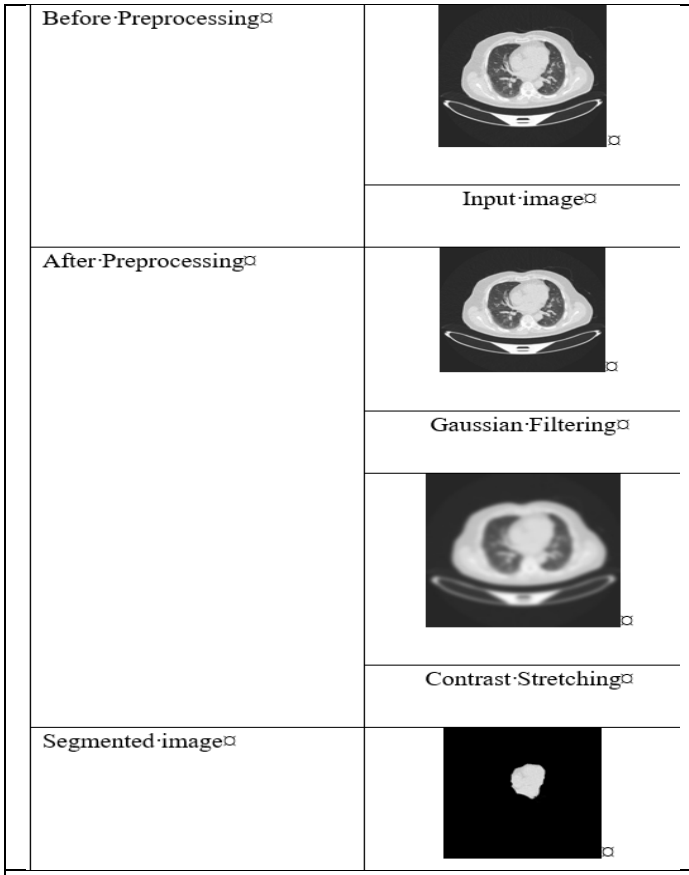

Fig. 3 Before and after preprocessing of the Bengin case

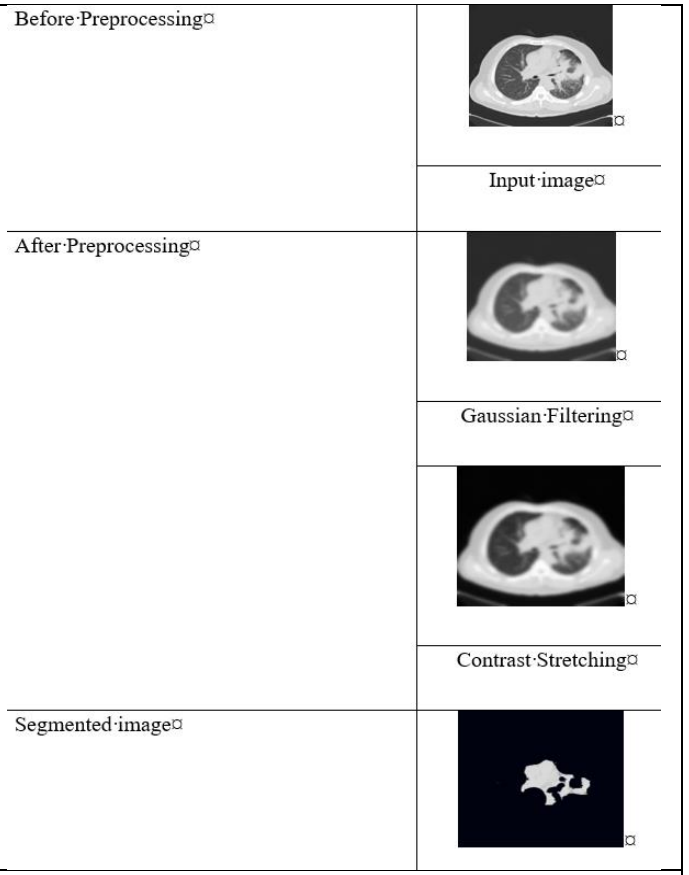

Fig. 4 Pictorial format of before and after preprocessing for the Malignant Case

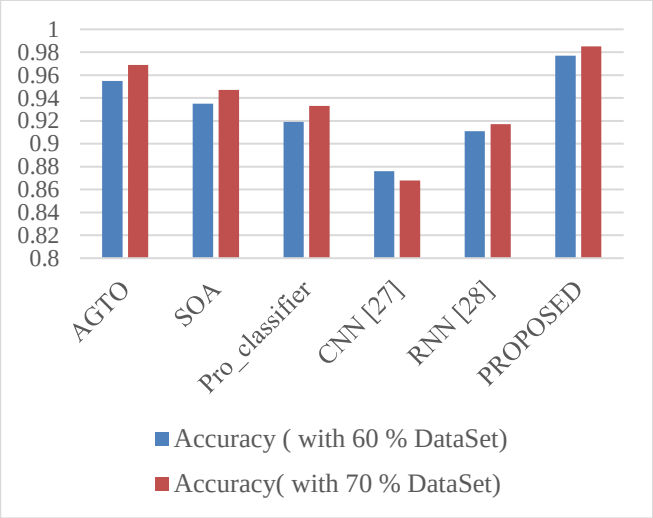

Fig. 5 Accuracy measures of the existing and proposed technique for the dataset with 60% and 70%

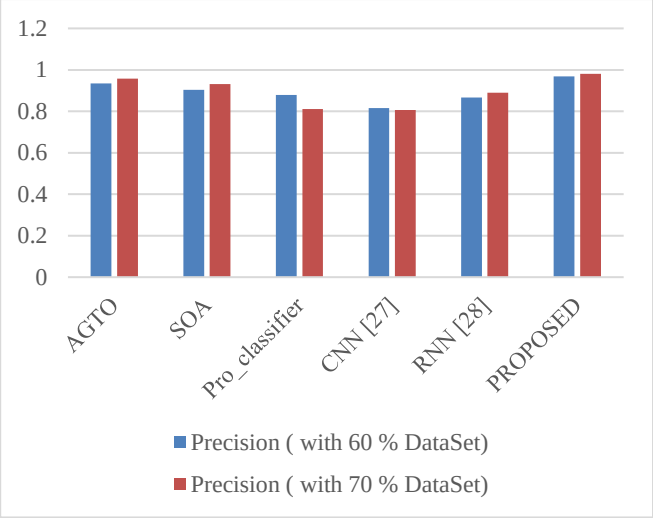

Fig. 6 Precision comparison of the existing and suggested method with 60% and 70% dataset

The graphical analysis of Tables 1 and 2 are depicted in Figures 5-13. Each metric was obtained with different values, which were useful for comparing the suggested approach. Every metric is explained separately in graphical form for datasets with two different trained set percentages. Figure 5 displays the accuracy measurement for several algorithms with the dataset for 60 and 70%. The accuracy values for algorithms AGTO, SOA, Pro_classifier, CNN [27], RNN [28], and suggested HYBDEEFU-FEASEG with 60% trained dataset are 0.955, 0.935, 0.919, 0.876, 0.911, and 0.977 respectively.

Accuracy with 70% trained dataset is listed as 0.969 for AGTO, 0.947 for SOA, 0.933 for Pro_classifier, 0.868 for CNN [27], 0.917 for RNN [28], and 0.985 for suggested method. In this accuracy measurement, the proposed model achieved the highest value of all existing models. Therefore, the newly constructed HYBDEEFU-FEASEG method presents great accuracy in bronchogenic carcinoma detection compared to existing approaches. Figure 6 shows the precision measurement for several methods with datasets for 60 and 70%.

The corresponding precision scores for the algorithms AGTO, SOA, Pro_classifier, CNN [27], RNN [28], and recommended HYBDEEFU-FEASEG with 60% trained dataset are 0.935, 0.903, 0.879, 0.8161, 0.867, and 0.969 respectively. The precision for each technique for the 70% training dataset is given as follows: AGTO: 0.957; SOA: 0.931; Pro_classifier: 0.811; CNN: 0.807; RNN: 0.890; and Suggested technique: 0.981. In this precision evaluation, the suggested model outperformed every other existing model.

Compared to other technologies, the newly developed HYBDEEFU-FEASEG method has good precision in detecting lung cancer. The sensitivity measurement for various approaches using datasets for 60 and 70% is shown in Figure 7 below. According to evaluation Table 1, the sensitivity values listed as 0.943, 0.907, 0.878, 0.815, 0.866, and 0.966 for the newly developed model, RNN [28], CNN [27], PRO_classifier, SOA, and AGTO respectively.

The proposed model reached the highest sensitivity with 60% of the trained dataset compared to other techniques. Based on Table 2, sensitivity values of 0.954 for AGTO, 0.921 for SOA, 0.911 for PRO_classifier, 0.803 for CNN [27], 0.875 for RNN [28], and 0.978 for the proposed approach. In this 70% trained dataset, the newly created technique also has the highest sensitivity rate. Thus, the proposed approach performs better than all existing techniques in 60 and 70 percentage of the trained dataset.

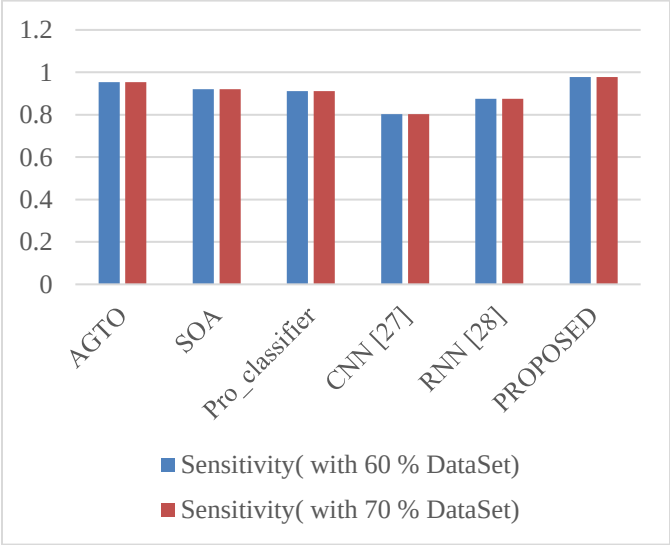

Fig. 7 Measures of sensitivity for the proposed and current techniques for datasets with 60% and 70%

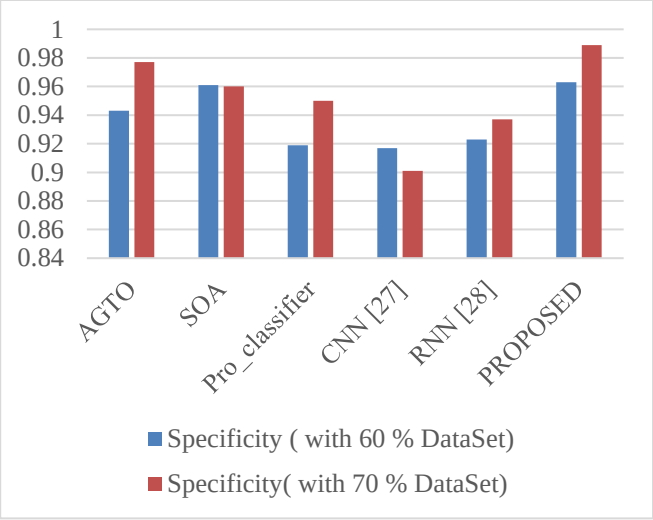

Fig. 8 Specificity comparison of suggested and current methods using 60% and 70% datasets

Figure 8 displays specificity assessment for several methodologies utilizing 60 and 70 percentage datasets. For the newly constructed model, AGTO, SOA, PRO_classifier, RNN [28], CNN [27], and, respectively, the specificity values are stated as 0.943, 0.961, 0.919, 0.917, 0.923, and 0.963. The suggested model had the maximum specificity compared to other methods using 60% of the training dataset.

According to Table 2, the specificity values for AGTO, RNN, SOA, PRO_classifier, CNN, and the suggested algorithm were 0.977, 0.960, 0.950, 0.901, 0.937, and 0.989 respectively. The newly developed method also has the greatest specificity value in this 70% trained dataset. Thus, the suggested strategy outperforms all other known techniques in 60 and 70 percent of the training dataset. The TPR assessment for various approaches using datasets for 60 and 70 percent is revealed in Figure 9 below.

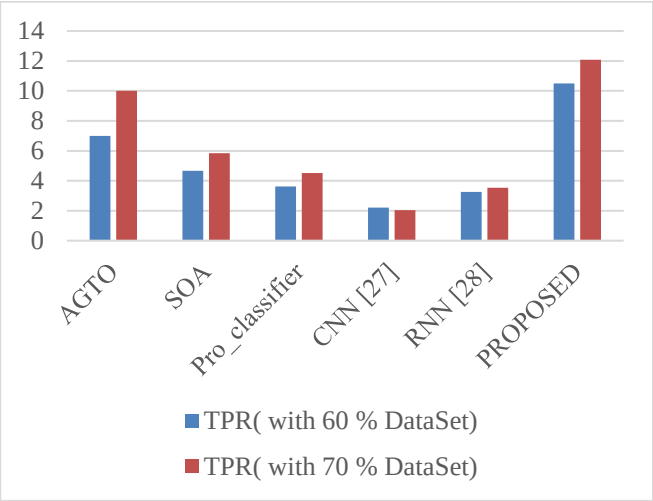

Fig. 9 Comparison of recommended and current approaches' TPR utilizing 60% and 70% of datasets

From the above TPR graphical representation, the resultant value for the dataset trained to 60 percentage are stated as 7.00, 4.656, 3.625, 2.04, 3,250 and 10.5 for techniques AGTO, SOA, PRO_classifier, CNN [27], RNN [28], and HYBDEEFU-FEASEG respectively. The values with 70% trained dataset are obtained as 10.00 for AGTO, 5.846 for SOA, 4.512 for PRO_classifier, 2.03 for CNN [27], 3.524 for RNN [28], and 12.071 for newly suggested approach. The developed method attains the highest value of TPR for these two sets of training data.

This indicates that the proposed model has a greater positive approach than all existing techniques. Therefore, this developed model is well suitable for lung cancer prediction. Figure 10 displays the FPR evaluation for several methodologies utilizing 60 and 70 percent datasets. According to Figure 10, the corresponding results for a dataset trained to 60% are 0.033, 0.048, 0.06, 0.092, 0.066, and 0.016 for algorithms AGTO, SOA, PRO_classifier, CNN [27], RNN [28], and HYBDEEFU-FEASEG, respectively.

A 70% trained dataset yielded the following values: 0.022 for AGTO, 0.039 for SOA, 0.051 for PRO_classifier, 0.098 for CNN [27], 0.062 for RNN [28], and 0.010 for a newly proposed technique with regard to these two sets of training data, the presented approach achieves the least FPR value. This shows that the suggested methodology is very beneficial compared to all other strategies already in use. As a result, our established model produces significantly less false values than other existing methods, and thus, the newly developed technique works effectively for predicting lung cancer.

The TNR evaluation for several approaches using datasets for 60 and 70 percent is shown in Figure 11. The Figure 11 shows the comparable results of methods AGTO, SOA, PRO_classifier, CNN [27], RNN [28], and HYBDEEFU-FEASEG for a dataset trained to a 60% TNR as 0.965, 0.951, 0.939, 0.907, 0.933, and 0.983, respectively. The following values were obtained from a 70% trained dataset: 0.977 for AGTO, 0.96 for SOA, 0.95 for PRO_classifier, 0.901 for CNN [27], 0.937 for RNN [28], and 0.981 for a recently developed method. The technique yields the highest TNR value for these two training data sets. This demonstrates that, compared to all other currently employed tactics, the methodology offered has a significantly advantageous approach.

Figure 12 displays the F1 score evaluation for several methods utilizing datasets for 60 and 70 percent. The results of the algorithms AGTO, SOA, PRO_classifier, CNN [27], RNN [28], and HYBDEEFU-FEASEG for a dataset trained to a 60% F1 score are displayed in the Figure 12 as 0.934, 0.905, 0.877, 0.810, 0.869, and 0.956 respectively.

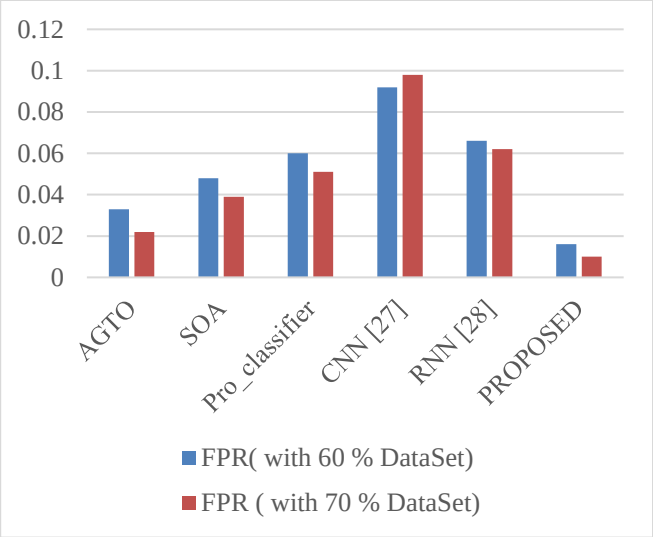

Fig. 10 FPR measurements for new and existing methods for datasets with 60% and 70%

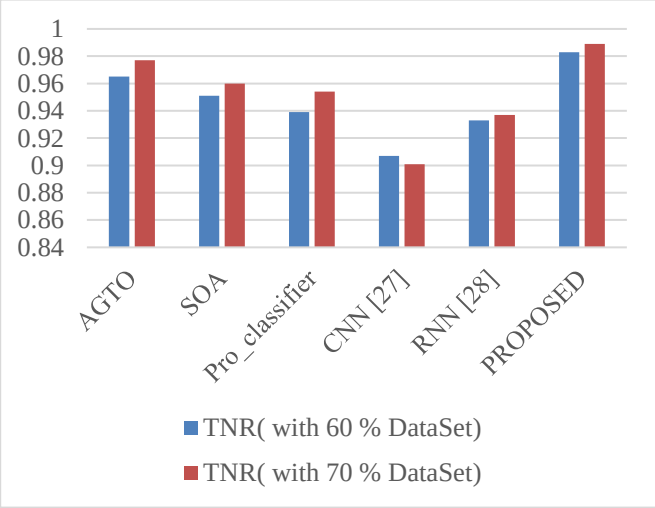

Fig. 11 Measures of TNR of proposed and current techniques for datasets with 60% and 70%

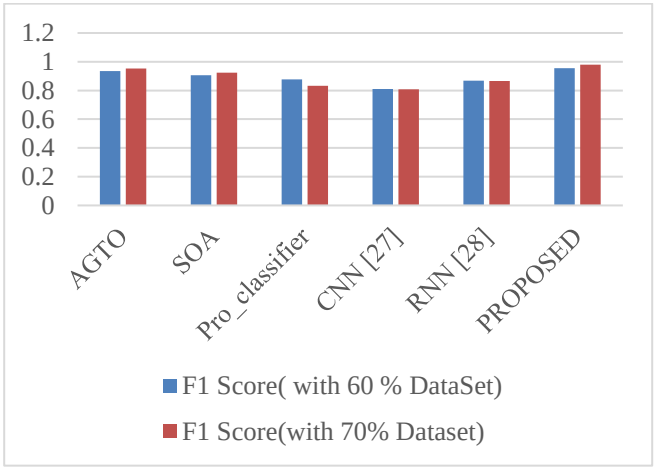

Fig. 12 F1 score measurements of current and planned methods for datasets with 60% and 70%

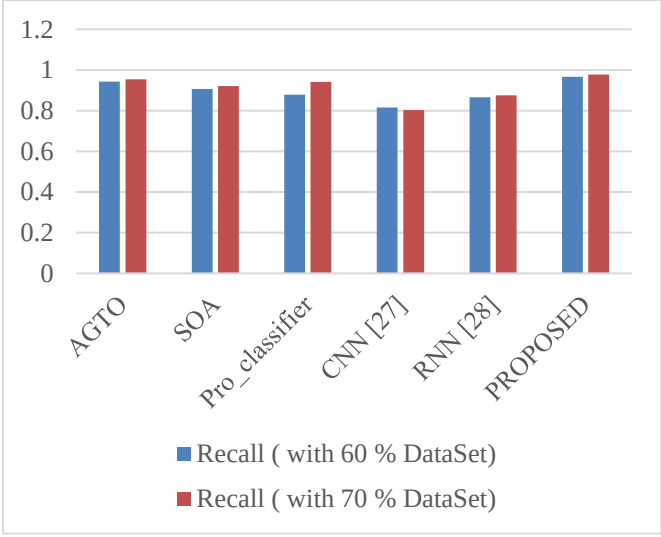

Fig. 13 Comparison of recommended and current approaches' recall utilizing 60% and 70% of datasets

A dataset that had been trained to 70% yielded the following values: 0.952 for AGTO, 0.807 for CNN [27], 0.833 for PRO_classifier, 0.867 for RNN [28], 0.923 for SOA, and 0.980 for a more modern technique. The suggested approach produces the greatest F1 score for these two training data sets. This implies that the methodology being supplied has a substantially more beneficial strategy when compared to all other currently used methods. The recall evaluation for various methodologies using datasets for 60 and 70 percent is shown in Figure 13. In Figure.13, the outcomes of the methods AGTO, SOA, PRO_classifier, CNN [27], RNN [28], and HYBDEEFU-FEASEG are shown as 0.943, 0.907, 0.878, 0.815, 0.866, and 0.966 for a dataset trained to a 60% recall, respectively. The following results were obtained using a dataset that had been trained to a 70% level: 0.954 for AGTO, 0.803 for CNN [27], 0.942 for PRO_classifier, 0.87 for RNN [28], 0.921 for SOA, and 0.978 for a more recent method. The recommended method yields the highest recall for these two training data sets. This suggests that, compared to all other approaches now in use, the methodology provided has a significantly more advantageous strategy.

5. Conclusion

In conclusion, the proposed HYBDEEFU-FEASEG approach offers a comprehensive and effective solution for accurate lung cancer detection, leveraging the power of deep learning and fuzzy logic integration. The five main stages of the model, including preprocessing, segmentation, feature extraction, feature selection, and lung cancer classification, synergistically contribute to achieving reliable and initial diagnosis of lung carcinoma. By utilizing DL and image processing technologies, the model demonstrates the capability to accurately classify and forecast lung cancer, providing valuable insights for promptly selecting the most

effective therapy. Integrating optimized SegNet for ROI identification and the hybrid optimization model for hyperparameter tuning enhances the segmentation process's accuracy and efficiency. The feature extraction and selection stages harness a combination of texture and shape-based features, ensuring comprehensive characterization of lung cancer images. The hybrid optimization approach refines feature selection, leading to the identification of the most relevant features for improved classification performance. Incorporating Bidirectional LSTM, CNN, and RNN classifiers and the subsequent input to the fuzzy logic stage further boosts the model's predictive power. The comparison with existing models using the IQ-OTH/NCCD dataset validates the efficiency and effectiveness of HYBDEEFU-FEASEG.

Future research will further focus on incorporating advanced deep learning techniques to enhance the model's accuracy and adaptability. Overall, HYBDEEFU-FEASEG holds great promise in supporting early and precise lung cancer diagnosis, ultimately contributing to better patient outcomes and advancing medical research in lung cancer detection.

Conflicts of Interest

The authors declare that they have no conflict of interest.

Funding Statement

No funds were received for this project

References

[1] Maryam Barzegar, "Niobium Incorporation In 2D MoSe2 For Lung Cancer Biomarkers Detection: The First-Principle Study Of Sensitivity Improvement," *Computational and Theoretical Chemistry*, vol. 1225, 2023. [CrossRef] [Google Scholar] [Publisher Link]

[2] Chang Gu et al., "A Cloud-Based Deep Learning Model in Heterogeneous Data Integration System for Lung Cancer Detection in Medical Industry 4.0.," *Journal of Industrial Information Integration*, vol. 30, 2022. [CrossRef] [Google Scholar] [Publisher Link]

[3] Zhiqiang Shen et al., "WS-LungNet: A Two-Stage Weakly-Supervised Lung Cancer Detection and Diagnosis Network," *Computers in Biology and Medicine*, vol. 154, 2023. [CrossRef] [Google Scholar] [Publisher Link]

[4] Arash Heidari et al., "A New Lung Cancer Detection Method Based on The Chest CT Images Using Federated Learning And Blockchain Systems," *Artificial Intelligence in Medicine*, vol. 141, 2023. [CrossRef] [Google Scholar] [Publisher Link]

[5] R. Sujitha, and V. Seenivasagam, "Classification of Lung Cancer Stages with Machine Learning Over Big Data Healthcare Framework," *Journal of Ambient Intelligence and Humanized Computing*, vol. 12, pp. 5639-5649, 2021. [CrossRef] [Google Scholar] [Publisher Link]

[6] Shreyesh Doppalapudi, Robin G. Qiu, and Youakim Badr, "Lung Cancer Survival Period Prediction and Understanding: Deep Learning Approaches," *International Journal of Medical Informatics*, vol. 148, 2021. [CrossRef] [Google Scholar] [Publisher Link]

[7] Ying Su, Dan Li, and Xiaodong Chen, "Lung Nodule Detection Based on Faster R-CNN Framework," *Computer Methods and Programs in Biomedicine*, vol. 200, 2021. [CrossRef] [Google Scholar] [Publisher Link]

[8] Xinxing Ju et al., "Factors Influencing The Preoperative Anxiety in Lung Cancer Patients Undergoing Video-Assisted Thoracoscopic Surgery: The Role of Information Needs, Illness Perception And Patient Trust," *Journal of Psychosomatic Research*, vol. 172, 2023. [CrossRef] [Google Scholar] [Publisher Link]

[9] R.L. Keith et al., "Lung Cancer: Premalignant Biology And Medical Prevention," *Seminars in Oncology*, vol. 49, no. 3-4, pp. 254-260, 2022. [CrossRef] [Google Scholar] [Publisher Link]

[10] Krishna Luitel et al., "Lung Cancer Progression Using Fast Switching Multiple Ion Beam Radiation and Countermeasure Prevention," *Life sciences in space research*, vo. 24, pp. 108-115, 2020. [CrossRef] [Google Scholar] [Publisher Link]

[11] S.K. Lakshmanaprabu et al., "Optimal Deep Learning Model for Classification of Lung Cancer on CT Images," *Future Generation Computer Systems*, vol. 92, pp. 374-382, 2019. [CrossRef] [Google Scholar] [Publisher Link]

[12] Giacomo Capizzi et al., "Small Lung Nodules Detection Based On Fuzzy-Logic and Probabilistic Neural Network with Bioinspired Reinforcement Learning," *In Proceedings IEEE Transactions on Fuzzy Systems*, vol. 28, no. 6, pp. 1178-1189, 2019. [CrossRef] [Google Scholar] [Publisher Link]

[13] Leila Akramian Arani, Frahnaz Sadoughi, and Mustafa Langarizadeh, "An Expert System to Diagnose Pneumonia Using Fuzzy Logic," *Acta Informatica Medica*, vol. 27, no. 2, pp. 103-107, 2019. [CrossRef] [Google Scholar] [Publisher Link]

[14] Rahul Boadh et al., "Study of Fuzzy Expert System for the Diagnosis of Various Types of Cancer," *Materials Today: Proceedings*, vol. 56, pp. 298-307, 2022. [CrossRef] [Google Scholar] [Publisher Link]

[15] Matthew D. Holbrook et al., "Detection of Lung Nodules In Micro-CT Imaging Using Deep Learning," *Tomography*, vo. 7, no. 3, pp. 358-372, 2021. [CrossRef] [Google Scholar] [Publisher Link]

[16] Alamin Talukder et al., "Machine Learning-Based Lung and Colon Cancer Detection Using Deep Feature Extraction And Ensemble Learning," *Expert Systems with Applications*, vol. 205, 2022. [CrossRef] [Google Scholar] [Publisher Link]

[17] Sahar Qazi, Naiyar Iqbal, and Khalid Raza, "Fuzzy Logic-Based Hybrid Models for Clinical Decision Support Systems in Cancer," *In Proceedings Computational Intelligence in Oncology: Applications in Diagnosis, Prognosis and Therapeutics of Cancers*, Springer Singapore, vol. 1016, pp. 201-213, 2022. [CrossRef] [Google Scholar] [Publisher Link]

[18] Weiping Ding et al., "FTransCNN: Fusing Transformer and a CNN based on Fuzzy Logic for Uncertain Medical Image Segmentation," *Information Fusion*, vol. 98, 2023. [CrossRef] [Google Scholar] [Publisher Link]

[19] Joel Valerian, and Dwi Seno Kuncoro Sihono, "Detection Of Suboptimal IMRT Treatment Plan Using Machine Learning on Radiomics Features of Dose Distribution For Lung Cancers," *Radiation Physics and Chemistry*, vol. 212, 2023. [CrossRef] [Google Scholar] [Publisher Link]

[20] Gai Li et al., "Study on The Detection of Pulmonary Nodules in CT Images Based on Deep Learning," *IEEE Access*, vol. 8, pp. 67300-67309, 2020. [CrossRef] [Google Scholar] [Publisher Link]

[21] Pasquale Ardimento et al., "Evo-GUNet3++: Using Evolutionary Algorithms to Train Unet-Based Architectures for Efficient 3D Lung Cancer Detection," *Applied Soft Computing*, vol. 144, 2023. [CrossRef] [Google Scholar] [Publisher Link]

[22] Yan Hua et al., "Autoantibody Panel on Small Extracellular Vesicles for the Early Detection of Lung Cancer," *Clinical Immunology*, vol. 245, 2022. [CrossRef] [Google Scholar] [Publisher Link]

[23] Shahab Ahmad et al., "A Novel Hybrid Deep Learning Model for Metastatic Cancer Detection," *Computational Intelligence and Neuroscience*, vol. 2022, no. 1, pp. 1-14, 2022. [CrossRef] [Google Scholar] [Publisher Link]

[24] Nasrullah Nasrullah et al., "Automated Lung Nodule Detection and Classification Using Deep Learning Combined With Multiple Strategies," *Sensors*, vol. 19, no. 17, 2019. [CrossRef] [Google Scholar] [Publisher Link]

[25] Amrita Naik, and Damodar Reddy Edla, "Lung Nodule Classification on Computed Tomography Images Using Deep Learning," *Wireless personal communications*, vol. 116, pp. 655-690, 2021. [CrossRef] [Google Scholar] [Publisher Link]

[26] Mustafa Bicakci et al., "Metabolic Imaging Based Sub-Classification of Lung Cancer," *IEEE Access*, vol. 8, pp. 218470-218476, 2020. [CrossRef] [Google Scholar] [Publisher Link]

[27] Abdulrazak Yahya Saleh et al., "Lung Cancer Medical Image Classification Using Hybrid CNN-SVM," *International Journal of Advances in Intelligent Informatics*, vol. 7, no. 2, pp.151-162, 2021. [CrossRef] [Google Scholar] [Publisher Link]

[28] Ahmed Maher Shaker, and Shengwu Xiong Lung, "Image Classification Based on Long-Short Term Memory Recurrent Neural Network," *International Conference on Emerging Electronic & Automation Technology ICEEAT*, China, vol. 2467, no. 1, 2023. [CrossRef] [Google Scholar] [Publisher Link]